

Research paper

Numerical estimations of lunar regolith trajectories and damage potential due to rocket plumes

Douglas Fontes^{a,*}, James G. Mantovani^b, Philip Metzger^a

^a Florida Space Institute, University of Central Florida, Partnership I, Research Pkwy, Orlando, FL, 32826, United States of America

^b Granular Mechanics and Regolith Operations Laboratory, NASA Kennedy Space Center, FL, 32899, United States of America

ARTICLE INFO

Keywords:

Rocket plume
Lunar particle
DSMC
Particle velocity
Particle trajectory

ABSTRACT

This study presents a numerical investigation of rocket plumes carrying regolith particles in the context of the lunar environment (gravity and vacuum conditions). We investigated two lander masses with a single rocket hovering at 5 different low altitudes perpendicular to a flat surface. For the regolith, we considered 9 particle sizes, with diameters from 1 μm to 1 cm. The initial condition of all particles was a null velocity at 0.3 m above the ground. The particles started at 19 different radial positions from the centerline of the rocket jet, 1 m to 10 m. We used a DSMC method to solve the rocket plume cases, considering the combustion product molecules from the propellant N_2O_4 +Aerozine 50. Steady-state plume flow solutions are one-way coupled with discrete particles, considering drag and weight forces. The results showed that particle angle is nearly constant for small ($d_p < 100 \mu\text{m}$) particles varying with initial radial position and lander altitude. Particle velocity is related to particle diameter as a power-law function and a Gaussian function of the initial particle position. Lander altitude and mass modulate the magnitude of particle velocity. Using the numerical solution data, we derived a numerical correlation for particle velocity that provides insight to avoid regolith abrasive blasting into the lunar lander, surrounding structures, and orbital satellites.

1. Introduction

Driven by economic opportunities, scientific knowledge, and space settlement, current space explorations aim to establish permanent structures on the Moon, Mars, and eventually other planetary bodies. The Moon is the closest extraterrestrial body for humans to settle permanent structures for exploration. Technology development to use extraterrestrial resources could reduce the dependency on Earth-based resources, promoting financially sustainable space exploration. In situ resource utilization (ISRU) is highly dependent on producing H_2O and O_2 for supporting life and H_2 and O_2 for fuel and propellant [1] for lunar missions. In this sense, ice reserves in lunar polar regions [2] may provide needed resources to supply drinking water, oxygen, and rocket fuel, as permanent structures are built on the Moon, reducing the dependence on Earth's resources. Permanent structures may require many spacecraft to repeatedly land directly on lunar soil before permanent landing site structures. Spacecraft landings without landing pads will create complex interactions between rocket plumes and the regolith (lunar particles), leading particulate ejecta to high velocities with significant hazard potential to the lander and surrounding structures. At the beginning of the lunar exploration program, some theoretical and experimental investigations about lunar soil properties and erosion [3,

4] recognized these issues. Depending on the rocket engine's approach, angle, lander mass, and geotechnical characteristics of the lunar soil, regolith particles may follow ballistic trajectories and velocities to cause damage to the landing spacecraft, hardware previously deployed in the vicinity, and even orbiting spacecraft, such as the Lunar Orbital Gateway. Lunar Surveyor III is an example of the damage potential caused by regolith blasted by the Apollo 12 lunar module rocket plume. Regolith blast from the lunar module rocket is considered the cause of surface damage of the Surveyor III, located approximately 160 m away from the landing site of the lunar module [5].

A better understanding of the mechanisms, characteristics, and conditions associated with rocket plume interacting with lunar regolith is crucial to mitigate potential damage from particle blasting of structures on the Moon. In a lunar environment, the hot rocket plume expands in the near-vacuum lunar environment, causing shock waves to interact with the lunar soil, with a high surface impingement pressure ($> 2000 \text{ Pa}$) that may promote cratering. The impinged plume jet reflects upwards, lifting eroded particulate and promoting a particle-laden compressible flow in the plume and soil interaction region [6]. The interactions between rocket plume and lunar soil are highly dependent on soil topology and properties, lander mass, crater evolution,

* Corresponding author.

E-mail addresses: douglashector.fontes@ucf.edu (D. Fontes), james.g.mantovani@nasa.gov (J.G. Mantovani), philip.metzger@ucf.edu (P. Metzger).

<https://doi.org/10.1016/j.actaastro.2022.02.016>

Received 17 June 2021; Received in revised form 19 January 2022; Accepted 19 February 2022

Available online 26 February 2022

0094-5765/© 2022 IAA. Published by Elsevier Ltd. All rights reserved.

and rocket angle affecting the faraway particle blast. In terms of soil displacement, Metzger et al. [7] summarizes four primary mechanisms: viscous erosion, bearing capacity failure, diffused gas eruption, and diffusion-driven flow. Not all of these mechanisms happen in specific cases. Whether a particular mechanism occurs depends on the environmental conditions and both the plume and soil conditions. Described by Bagnold [8], the first mechanism consists of the displacement of the top layer of grains by shearing forces of the flow over the granular material. Bearing capacity failure is the bulk shearing of the soil to form a cup, beneath a localized mechanical load applied to the surface. In this mechanism, the high-pressure region directly under the thruster's impingement point shoves the soil downward [3]. In the diffused gas eruption mechanism, gas flows into soil pores driven by stagnation pressure. This gas flow transfers soil to another location over time [9]. The diffusion-driven flow occurs when the stagnation pressure of the plume flow drives gas through the ground. The gas within the soil acts as a distributed body force, causing it to fail and shear perpendicularly to the surface of the soil [10]. Bearing Capacity Failure differs from diffusion-driven flow because it puts most of the force directly on the surface of the soil, whereas diffusion-driven flow distributes the force throughout the bulk of the soil, and this results in a different flow pattern as the soil moves to form a crater. Viscous erosion is the most likely soil displacement mechanism in lunar landings because of the high compaction of the soil and lack of background atmosphere. The rocket plume in the lunar environment is highly under-expanded, acting on a large soil area. However, other cratering mechanisms may occur in massive landers devoted to establishing permanent human settlements.

Given the difficulty to experimentally analyze the interactions between rocket plume with regolith in the lunar environment, several researchers have investigated this two-phase flow problem numerically using different modeling levels [7,10–19]. In lunar conditions, plume flow may not comply with the continuum hypothesis because of the near-vacuum condition. In this case, continuum-based codes, i.e. Navier–Stokes equations [20], fail to predict the plume flow. Thus, unless the rocket nozzle exit is sufficiently close to the soil and the region of analysis is constrained to the continuum region, a Boltzmann equation solver must be considered, such as the direct simulation Monte Carlo (DSMC) method [21]. The DSMC method stochastically solves the trajectory of computational parcels (representing gas molecules), interacting with each other and surfaces. The DSMC flow solution can be either one or two-coupled with particulate to describe the behavior of the gas and granular phases. Different coupling solutions may differ significantly depending on the plume and particulate conditions. Besides coupling type, physical conditions influence flow and particle behaviors. For instance, crater formation results in different predictions of rocket plume flow and particle trajectories. Lane et al. [22] numerically investigated how different crater configurations affect rocket plume flows and particulate trajectories. The authors analyzed particle trajectories for different rocket nozzle heights, considering craters placed at a certain distance from the centerline using DSMC and Navier–Stokes-based solvers. Their particle velocity and angle predictions agreed well with dust angles from Apollo landing videos [23]. When the authors placed a crater 15 rocket nozzle radii from the centerline, they found that 100 μm particles were affected by the flow changes caused by the presence of a crater, while particles diameters above 250 μm would follow ballistic trajectories. In their model, Lane et al. [22] obtained particle velocities of up to 1500 m/s for a 10 μm diameter particle, and approximately 200 m/s for a particle of 500 μm in diameter. Lane et al. [22] found that far from the plume interaction region, particles followed ballistic trajectories in angles between 1 – 3 degrees relative to the horizontal surface. Morris et al. [15] considered one-way and two-way couplings using a hybrid approach based on a Navier–Stokes solver for the rocket exit near-field and a DSMC method for the far-field. Two-way coupled simulations assume that the particles affect the flow as a reaction of the flow affecting particles, while in a

one-way coupled simulation, the flow does not perceive particles. In the context of rocket plume ejecting lunar particles, a one-way coupling strategy results in higher gas and particle velocities. Morris et al. [15] investigated spherical particles of six diameters (200 nm, 800 nm, 2 μm , 5 μm , 8 μm , and 11 μm) for a lander hovering at 2 – 5 m above the ground. The authors found that the dust sprays are sensitive to grain–grain collisions. The restitution coefficient for colliding grains showed a significant impact on how grain–grain collisions scatter the dust sprays. In a coupled simulation, the dispersed particles decrease the gas velocity and thicken the boundary layer, decreasing the overall particle velocity. For instance, considering fluid–particle coupling, a 2 μm size particle reached up to 945 m/s for one-way coupled simulation compared to 740 m/s for two-way coupling. Another work investigated plume soil interaction as a two-way coupled simulation using macroscopic and microscopic aerodynamic methods [16]. The macroscopic method considers the gas as a continuum phase interacting with discrete particles, while the microscopic considers interactions of discrete gas molecules on particle surfaces. The numerical model of Li et al. [16] consists of an axisymmetric domain with a 0.8 m rocket exit diameter, placed 1.4 m above the bottom surface, and a radial dimension of 15 m. Due to the low hovering altitude, their simulations resulted in higher particle angles, up to 32.8 degrees for a 10 μm size particle, compared to the values measured from video analyzes from Apollo landing (1 – 3 degrees). These different studies predicted velocities of the ejecta particles that were in wide disagreement, by as much as 900 m/s in the particle velocity prediction using the considered methods.

The ability of the scientific community to model, predict, and analyze rocket plumes interacting with lunar particulates has improved significantly since the Apollo era. However, current methods are still not able to correctly predict the mechanisms associated with it. On the other hand, it is practical to estimate particle velocity, angles, and trajectories for further lunar exploration advancements, including establishing parameters to avoid damage to surrounding structures. In this context, the purpose of the present work is to present crucial information on particles leaving the plume region, such as velocity, angle, and trajectory. We derive useful functions conveniently relating particle velocity data to lander mass, hovering altitude, particle diameter, and initial radial position. The numerical model uses the DSMC method to solve the rocket plume flow, while particle trajectories were solved one at a time using a discrete particle solver based on Newton's second law. The results and analysis in this study provide practical and insightful information about particles interacting with rocket plumes in the context of the lunar environment.

The manuscript is organized in five sections, as follows: Section 2 presents the physical model with the assumed hypothesis and boundary conditions for both the flow of the rocket exhaust gases and the single-particle trajectory; Section 3 presents the mathematical and numerical models used to solve rocket plume and particle interaction; results and analysis of the considered cases are detailed discussed in Section 4 and; Section 5 presents the final remarks of this study.

2. Physical description

To model the plume jet flow in the lunar environment, we considered a single rocket nozzle whose nozzle exit is directed perpendicularly to a flat surface. Given the symmetry of the problem, we could consider an axisymmetric plane only. However, the `dsmcFOAM` code, `OpenFOAM-v2006`, does not solve axisymmetric geometries. Thus, to reduce the computational cost of a full 3D model, we limited the geometry to one-quarter of a cylindrical region. The quarter domain is 10 m height and 20 m in radius. The lander altitude, l_h , is defined as the distance between the rocket nozzle exit and ground surface and varies from 1 to 7 meters. Fig. 1 presents the physical model diagram, indicating the boundary conditions associated with each surface and the dimensions.

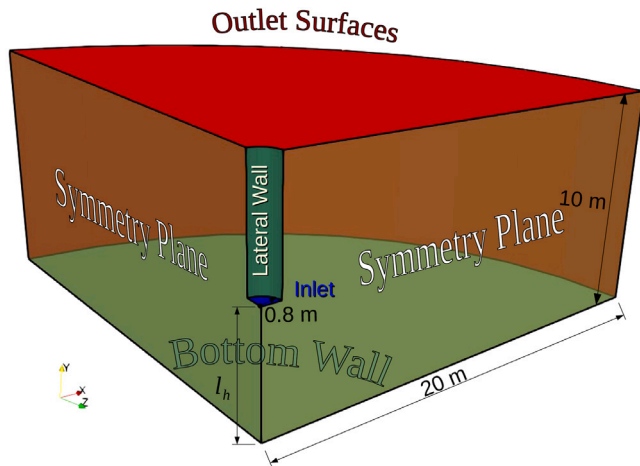


Fig. 1. Schematic diagram of the physical domain adopted for the numerical simulations.

Discrete particles statistically represent the interactions of combustion product molecules to obtain average flow solutions of the rocket plume. The molecules are from the combustion products of a stoichiometric reaction of the propellant N_2O_4 + Aerozine 50, where Aerozine 50 constitutes 50% of N_2H_4 and 50% of $C_2H_8N_2$. The rocket plume impinges on the ground surface, which is assumed to be a non-penetrable, no-slip surface. Because of the near-vacuum condition, the gas expands in all directions reducing density and increasing velocity, which creates shock waves that interact with the bottom surface and surrounding environment. The boundary conditions for the gas flow are as follows:

- Bottom and lateral walls: no-slip condition, with constant temperature from the average lunar soil temperature (200 K);
- Symmetry Plane: symmetry condition;
- Outlet Surfaces: outflow condition and;
- Inlet: velocity of 3050 m/s and static gas temperature of 3000 K crossing perpendicularly the surface, based on propellant characteristics in vacuum, such as specific impulse in vacuum ($I_{sp} = 311$ s) Braeunig [24].

After solving for the gas flow, the trajectories of the ejected lunar soil particles are calculated (as described below) based on the drag force and the particle weight in lunar gravity, which are the main forces responsible for a lunar plume–soil interaction. Particle weight equals lunar gravitational acceleration, 1.62 m/s^2 multiplied by the particle mass. Drag force is related to the drag coefficient, calculated through the empirical drag coefficient presented by Lane et al. [22]. When a particle collides with any surface, except outlet surfaces, it reflects in a perfectly elastic collision. The single-particle trajectory simulation finishes when the calculations reach the final solution time or when a particle escapes the domain through outlet surfaces.

For the present study, we considered two different lander masses (10525 and 40 000 kg, henceforward termed as 11 and 40 ton landers to represent an Apollo lander and a current human scale lander, respectively) and five rocket altitudes (1, 2, 3, 5, 7 m). For the single-particle trajectory cases we considered 9 particle sizes (1.0×10^{-6} , 5.0×10^{-6} , 1.0×10^{-5} , 5.0×10^{-5} , 1.0×10^{-4} , 5.0×10^{-4} , 1.0×10^{-3} , 5.0×10^{-3} , 1.0×10^{-2} m) and 19 initial radial positions (1.0 : 0.5 : 10.0 m) inside the domain. In all cases, particles initiate 0.3 m above the bottom wall surface. We adopted this initial particle position due to the limitations of solving the boundary layer, soil irregularities, and erosion mechanisms that would result in particle lifting. To accurately model the boundary layer of the gas flow interacting with particulate soil, a continuum flow solver for low Knudsen number regions, transferring information

from/to the DSMC method, is necessary to provide accurate and computationally feasible solutions. Moreover, the erosion process involves particles rolling and bouncing in the boundary layer, thus affecting it. This complex interaction requires a two-way coupling between phases and ground surface modification due to material removal. We recognize that the lack of a better representative model to solve soil–plume interactions is the main reason for discrepancies in particle velocities and trajectories [12,13,15]. However, our numerical modeling provides a broader analysis of particles ejected by landers at different altitudes and convenient correlations for particle velocity for the investigated ranges.

3. Mathematical and numerical modeling

In the present study, the plume flow cases are highly rarefied, violating the continuum hypothesis. The continuum hypothesis limits are associated with the Knudsen number, which is the ratio of the molecular mean free path length to a representative physical length scale, $Kn = \frac{\lambda}{L}$. The molecular mean free path length can be estimated as $\lambda = \frac{1}{\sqrt{2}n_v d}$, where d is the mean diameter of the molecule and n_v is the number density. Although an overall representative flow dimension can represent the length scale, it may misrepresent the rarefaction degree in certain regions. Using a scale length based on macroscopic gradients, such as the ratio between density and the magnitude of the density gradient, better represents the local degree of rarefaction through the Knudsen number. Thus, we calculated the local length scale as the ratio of the density and the magnitude of density gradient in the domain, $L = \frac{\rho}{|\nabla \rho|}$. The Knudsen number threshold for using a macroscopic

approach is $Kn < 0.1$ [21]. A mathematical model based on the continuum hypothesis fails to properly solve the plume flow since the Knudsen number is higher than that threshold in a large region of the physical domain for the cases in this study, as shown in Section 4. A microscopic approach can appropriately model the flow behavior of the gas flow in a rarefied condition. The microscopic approach or molecular model considers the molecule structure and degrees of freedom to determine the state of the molecule in a specific position at any time. The microscopic approach requires high computational resources since it performs calculations for all or a sufficient statistical sample of the molecules to represent the flow. To solve the flow with the microscopic approach, a model derived from the Boltzmann equations must be used, Eq. (1),

$$\frac{\partial(nf)}{\partial t} + \mathbf{c} \frac{\partial(nf)}{\partial \mathbf{r}} + \mathbf{F} \frac{\partial(nf)}{\partial \mathbf{c}} = J(f, f^*), \quad (1)$$

where: nf is the product of the number density and the normalized molecular velocity distribution function; \mathbf{c} is the velocity vector of the molecule; \mathbf{r} is the position vector of the molecule; \mathbf{F} is an external force and; $J(f, f^*)$ is a nonlinear integral that describes the binary collisions, in which the superscript $*$ represents post-collision properties [25].

The direct simulation Monte Carlo (DSMC) method, proposed by Bird [21], uses a stochastic approach to solve the Boltzmann equation, which considerably reduces the computational cost compared to solving all molecules, which is known as a direct simulation of the Boltzmann equation. The DSMC model considers computational parcels, representing statistically several molecules, to solve intermolecular and molecular-surface collisions. In the present investigation, all simulations use the variable hard sphere (VHS) molecular model for binary collisions [26]. Energy exchanges between particles and wall surfaces are solved by the Maxwell thermal model [21]. The simulations in the present work were solved using the dsmcFoam solver from OpenFOAM [27].

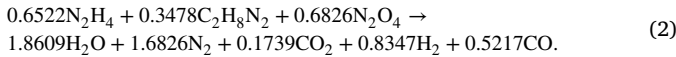
Local average calculations of molecule velocity and collisions are required to analyze the flow through mean flow variables. We considered the molecules of the combustion products of a stoichiometric reaction of the propellant N_2O_4 + Aerozine 50 for the computational

Table 1

Number density of molecules injected in the numerical domain according to the mass lander.

| Molecule | Molar mass [g/mol] | Combustion product [%] | Number density [$\times 10^{22} \text{ m}^{-3}$] | |
|------------------|-----------------------|---------------------------|--|---------------|
| | | | 11-ton lander | 40-ton lander |
| H ₂ O | 18 | 36.67 | 0.8617 | 3.275 |
| N ₂ | 28 | 33.16 | 0.7793 | 2.962 |
| H ₂ | 2 | 16.45 | 0.3866 | 1.469 |
| CO | 28 | 10.29 | 0.2418 | 0.919 |
| CO ₂ | 44 | 3.43 | 0.0806 | 0.3063 |

parcels (statistical representation of a high number of actual molecules) injection through the rocket exit surface according to Eq. (2),



Thus, we selected the number density at the inlet condition such that the resulting thrust equaled the weight of the lander in lunar gravity. Table 1 shows the properties and quantities associated with the combustion product molecules injected in the numerical domain for each of the 11 and 40 ton landers.

To ensure steady state convergence, we evaluate variations on flow field variables. Comparisons of flow solutions at different instants showed that a final solution time of 3 s using $\Delta t = 10^{-5}$ s ensured statistical convergence to steady state solutions. Despite using the computational parcel strategy to statistically represent actual molecules at the microscopic level, the DSMC method is still computationally expensive, for it solves displacements and collisions for all computational parcels. Considering a 3 s flow solution and a time step of 10^{-5} s, each case took nearly 7 days to finish using 32 Intel Xeon® processors of Stokes cluster from the University of Central Florida.

Via a Lagrangian approach, regolith particles are transported by the previously solved gas flow fields using one-way coupling. Particle trajectory is solved using Newton's second law, considering drag (F_{d_i}) and weight (F_{w_i}) forces. Particle velocity and position are obtained from the solution of the ordinary differential equation, Eqs. (3) and (4),

$$m_p \frac{du_{p_i}}{dt} = F_{d_i} + F_{w_i}, \quad (3)$$

$$\frac{dx_{p_i}}{dt} = u_{p_i}, \quad (4)$$

where: the subscript p refers to particle; u and x are, respectively, the particle velocity and position; m is the particle mass and; subscript i indicates the three components of a vector. We neglected lift, virtual mass, and Basset forces since they are less relevant in this type of interaction or are not well established. We also neglected electrostatic effects on dust particles. Dusty plasmas occur on the surface of the Moon as described by Popel et al. [28]. Although electrostatic forces may affect the initial detachment of dust particles from the bottom surface, the present investigation did not consider such effects but recognized the necessity of further studies.

The drag force is calculated according to the Eq. (5),

$$F_{d_i} = m_p \frac{3\rho C_D}{4\rho_p d_p} |u_{i,t} - u_{p_i}| (u_{i,t} - u_{p_i}). \quad (5)$$

The drag coefficient, C_D , is calculated from an empirical correlation [22], which yields Eq. (6),

$$C_D = \begin{cases} 24.0 Re^{-1} & Re < 2 \\ 18.5 Re^{-0.6} & 2 \leq Re < 500 \\ 0.44 & Re \geq 500 \end{cases} \quad (6)$$

where, $Re_p = \frac{\rho |u_i - u_{p_i}| d_p}{AT\beta}$ is the droplet Reynolds number. T is the local static temperature of the gas at the particle's position, and A and β are empirical parameters, set as $A = 1.71575 \times 10^{-7}$ and $\beta = 0.78$. The

combined buoyancy–weight force is calculated according to the Eq. (7),

$$F_{w_i} = \left(1 - \frac{\rho}{\rho_p}\right) m_p g_i. \quad (7)$$

Considering the transport of a single particle, we implemented a numerical code in python that uses that gas flow to transport particulate. The code uses a tracking algorithm that sweeps the numerical cells to find the closest centroid cell to the particle position. Hence, the drag force associated with the plume flow is calculated based on the flow variables in that position. We used a Runge–Kutta 4th order integration scheme and a time step of $\Delta t = 10^{-4}$ s, to solve particle position and velocity, ensuring particle trajectory solution independent of time-step. We included the flow chart of the particle transport python code in the Appendix.

4. Results and discussions

This section presents rocket plume flow and particle trajectory results for the defined cases in the physical description section. Firstly, we discuss rocket plume flows results obtained by the DSMC method. The second subsection deals with particle trajectory analysis based on rocket plume flows. Finally, the third subsection describes a correlation for particle velocity out of plume flow influence based on the numerical results.

4.1. Rocket plume flow

Fig. 2 shows the rarefied flow condition for the highest lander altitude of the considered cases based on local Knudsen fields.

As the lander is closer to the bottom surface, the local Knudsen number significantly reduces in the domain. However, it remains high in the surroundings of the upper wall surfaces.

For the sake of clarity, we present flow results for landers at the lowest (1 m) and highest (7 m) altitudes only, without losing understanding of trends and behaviors of the investigated altitude range. Despite of the lack of experimental data for validation, the results of this work present similar flow characteristics regarding shock wave structures, velocity, density, temperature and pressure fields have been reported in other studies [11,13,29].

Fig. 3 presents the velocity magnitude fields of rocket plumes. Due to the near-vacuum condition, the gas rapidly expands, forming a particular surface shock wave in the form of a bowl. The impingement point beneath the bowl shock wave creates a favorable pressure gradient in the radial direction that induces high velocity outward radially. Also, the collision of gas molecules with the bottom surface promotes a reflected flow upwards. As the lander descends, the reflected shock wave angle increases because the plume momentum becomes mainly normal to the soil surface. As the lander is closer to the ground, the plume does not fully expand in the analyzed region, resulting in lower velocity values. The plume flow expands faster for an 11-ton lander, resulting in slightly higher maximum velocities than a 40-ton lander.

The rocket plume pressure field promotes forces acting perpendicularly to the lunar surface, leading to surface regolith erosion by different mechanisms [7]. Thus, the pressure field is an important metric to understand how the soil may support such distributed loading and what locations are mostly affected. Fig. 4 depicts pressure fields for 11 and 40 ton landers at 1 and 7 meters in altitude. As expected, the 40-ton lander produces a plume with higher pressure levels than the 11-ton lander. The maximum pressure ratio (3.70) due to the landers is nearly the landers mass ratio (3.80). Two flow regions are present when the lander is at 7 m: conical expansion in the jet stream direction; and bulb flow development in the radial direction. In the jet stream direction, the pressure reduces rapidly from the rocket exit due to vacuum expansion. The pressure recovers as the flow impinges on the bottom surface. The plume pressure on the surface is higher than the

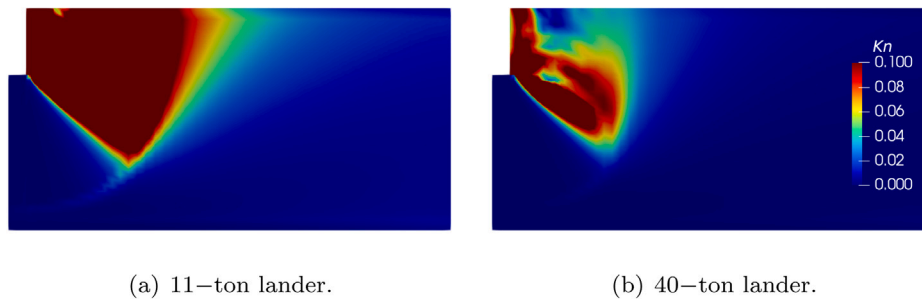


Fig. 2. Local Knudsen number for different lander masses hovering at 7 meters in altitude.

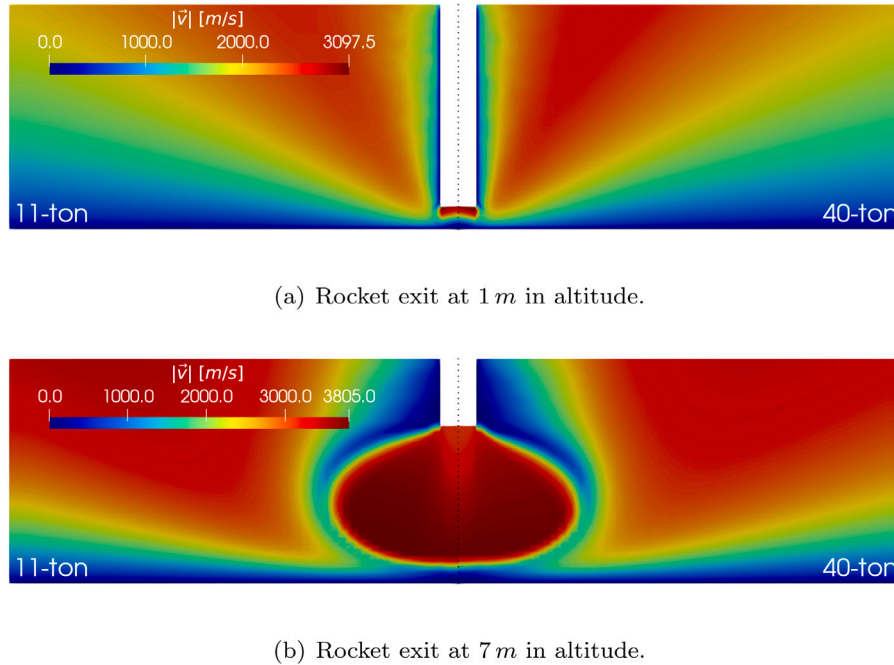


Fig. 3. Velocity magnitude fields for different lander masses and altitudes.

pressure at the rocket exit when the lander is at 1 m in altitude due to the short expansion distance, which converts the momentum flux from the orthogonal gas flow into stagnation pressure.

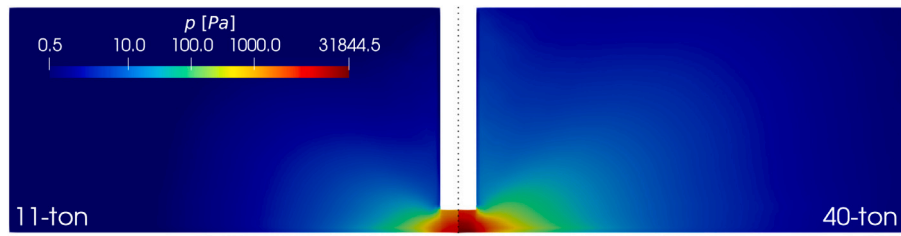
In the context of a rarefied atmosphere, the rocket plume flow density plays a significant role in particle transport, mainly dominated by drag forces. Density assumes the highest values close to the rocket exit and the impingement region. Low inertia particles rapidly follow the flow velocity and direction. These accelerated particles are weakly influenced by the flow downstream because the gas rapidly reaches low-density values (below 10^{-5} kg/m³) when moving away from the centerline, as depicted in Fig. 5. The radial change in density is highly associated with the lander's altitude. As the lander approaches the bottom surface, the rocket jet presents less radial expansion, which causes a higher radial gradient of density on the bottom surface. For instance, considering an 11-ton lander, while the ratio between densities on the bottom surface at the centerline and 5 rocket exit radii from the centerline is approximately 50 for the lander at 1 m from the bottom surface, this same ratio is 2.4 for the lander at 7 m in altitude. As expected, the 40-ton lander produces a plume with a higher density than the 11-ton lander. Similarly to the pressure, the maximum density ratio (3.60) due to the landers is nearly the landers mass ratio (3.80).

Fig. 6 shows temperature fields for both landers at the highest and lowest altitudes. The highest temperature of the flow occurs in the shock wave due to the abrupt property changes. There is a high-temperature gradient on the bottom surface, caused by the imposed

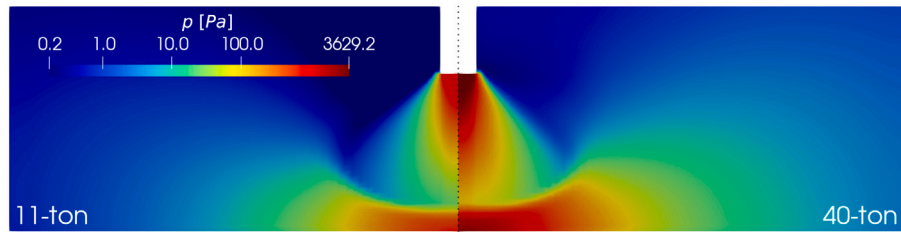
boundary condition of constant temperature. This high gradient may affect the transition to turbulence and the boundary layer in the continuum region. However, the mesh resolution and numerical model used in the present investigation cannot accurately capture the boundary layer development. Comparing the maximum temperature between lander masses, the maximum temperature difference increases as the lander's altitude reduces. At 7 m, the maximum temperature difference between 40-ton and 11-ton landers is approximately 66 K, whereas, at 1 m in altitude, the maximum difference temperature is nearly 334 K. These differences are associated with the higher number of molecules interacting with each other in the shock wave, as the lander mass increase and the lander elevation decreases.

The rocket jet imposes normal and tangential loading that influence the erosion process and lifting of particles from the soil. Although, the physics and modeling of plume surface interactions are challenging, pressure and shear on the flat surface case provide a better understanding of initial mechanisms and instabilities that promote soil erosion and lifting of particles. The flat surface configuration also represents well the conditions expected in hard soil and landing pad cases. In Fig. 7, each quadrant depicts the bottom surface pressure distribution for a different lander altitude. When the lander is closer to the ground, the impingement area becomes smaller and the maximum pressure higher. Also, the pressure on the surface is directly related to the lander mass.

In the same view, Fig. 8 shows the shear stress on the bottom surface for both landers at different altitudes. The maximum shear

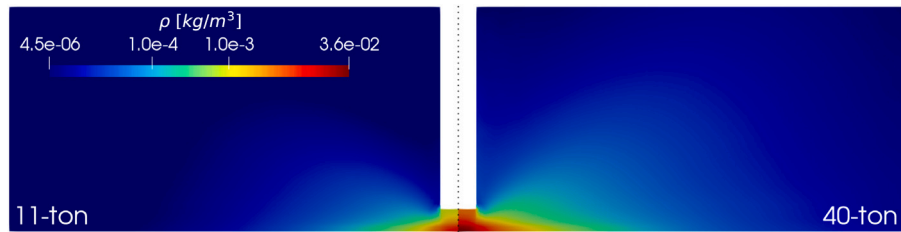


(a) Rocket exit at 1 m in altitude.

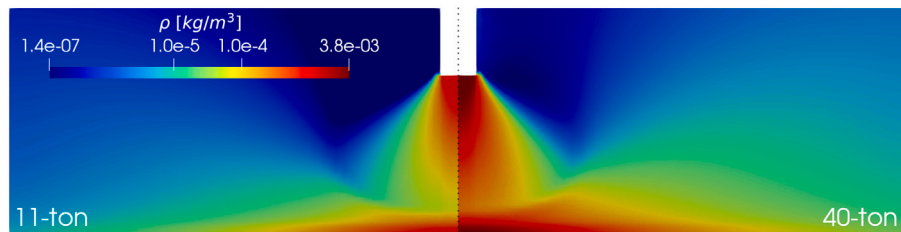


(b) Rocket exit at 7 m in altitude.

Fig. 4. Pressure fields for different lander masses and altitudes.



(a) Rocket exit at 1 m in altitude.



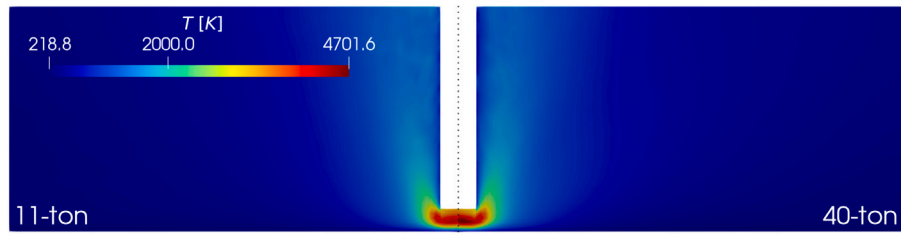
(b) Rocket exit at 7 m in altitude.

Fig. 5. Density fields for different lander masses and altitudes.

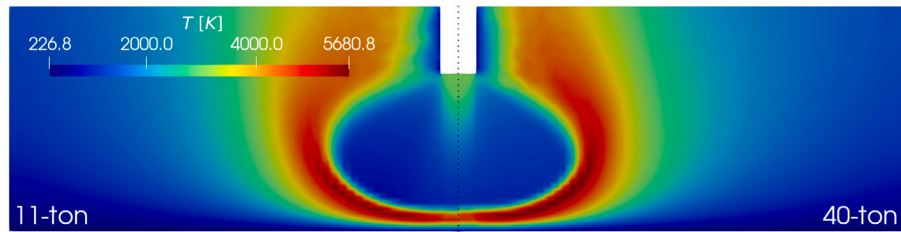
stress occurs at a certain distance from the centerline. According to the Roberts [30] model, this distance occurs when the dimensionless distance, ζ , is equal to the unity.¹ The distance of maximum shear stress occurs approximately 0.4 times the rocket nozzle altitude using the typical thrust flow values from Roberts [30]. In another study [11], results obtained from a hybrid model using DSMC and a solver based on Navier–Stokes showed maximum shear stress at a radial distance from the centerline is approximately half of the altitude. In the present

¹ The x-axis of Fig. 3 in Roberts [30] paper is not using the correct variable, ζ .

simulations, the shear stress peak did not relate to the elevation, which may be associated with the considered low altitude range. For lower altitudes, the jet impinges more perpendicularly to the surface. Thus, variations in the shear stress peak are less dependent on lander altitude. Fig. 9 shows comparisons of the surface shear stress profiles from the present simulations and from Roberts [30] model, which considered the surface drag coefficient associated with the use of hemispheric protuberances to represent the roughness of the lunar surface with a drag coefficient of 0.2. Morris et al. [11] used a drag coefficient of 1.0, suggesting roughness scales comparable to the boundary layer thickness. According to the authors, a unitary drag coefficient presented a better prediction of erosion rate estimations associated with Apollo

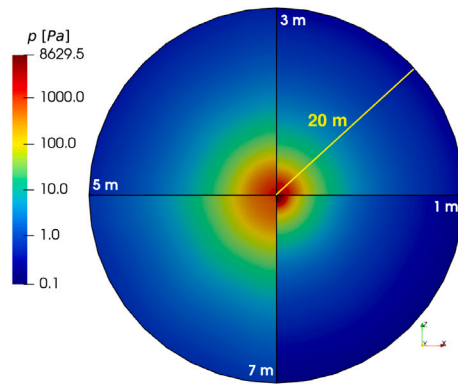


(a) Rocket exit at 1 m in altitude.

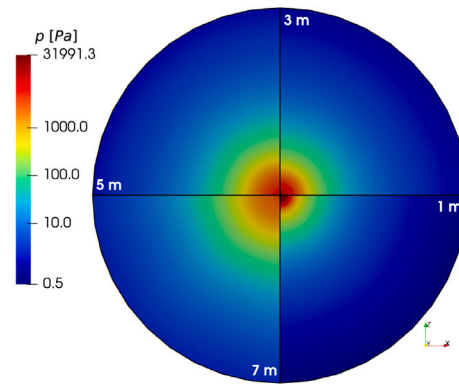


(b) Rocket exit at 7 m in altitude.

Fig. 6. Temperature fields for different lander masses and altitudes.

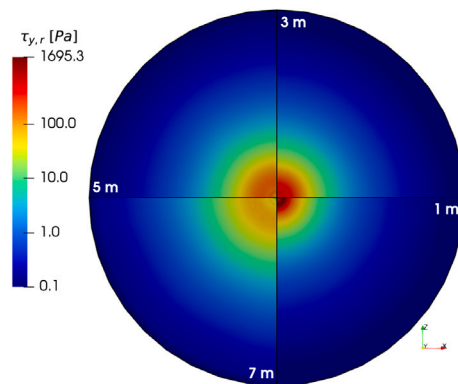


(a) 11-ton lander.

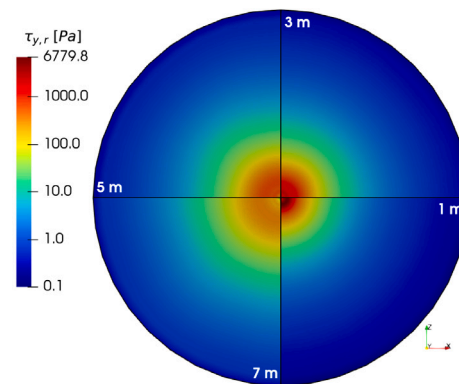


(b) 40-ton lander.

Fig. 7. Pressure on the bottom surface for different lander masses and altitudes.



(a) 11-ton lander.



(b) 40-ton lander.

Fig. 8. Shear stress on the bottom surface for different lander masses and altitudes.

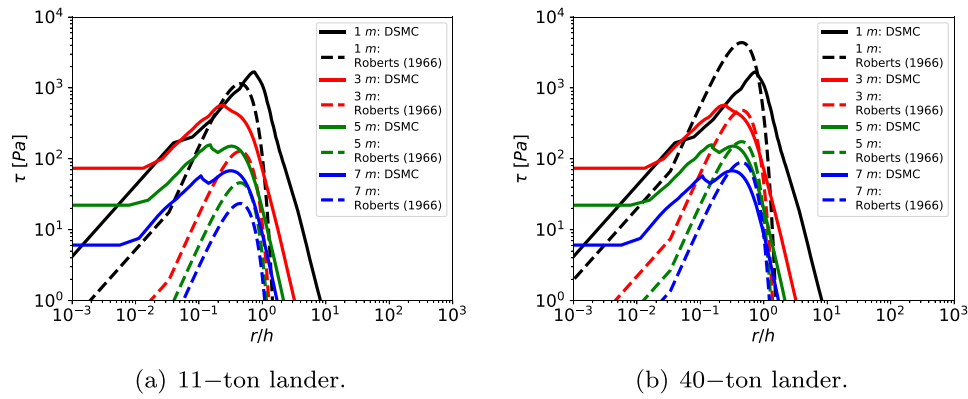


Fig. 9. Shear stress profiles on the bottom surface for different lander masses and altitudes.

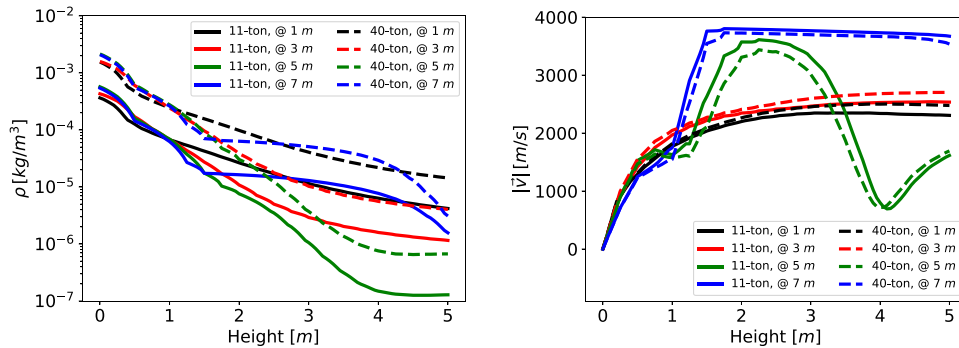


Fig. 10. Vertical profiles of density and velocity for different lander masses and altitudes.

missions. However, this parameter should not be constant since it depends on the boundary layer characteristics associated with the lander's altitude. Thus, a detailed solution of the boundary layer flow is required to calculate more accurately the drag coefficient as a function of the flow conditions.

Given that the drag force acting on particulate is directly related to the density and velocity of the rocket plume, we extracted vertical and radial line probes from the numerical solutions to understand the flow behavior and differences for different lander altitudes and masses. Fig. 10 shows density and velocity magnitude vertical profiles. The vertical profile is a vertical line of 5 m in length is placed 4 rocket diameters from the centerline. In these profiles, we can see the flow property changes associated with the shock wave. For lander altitudes at 5 and 7 meters, the vertical profiles intersect the shock wave, which results in abrupt variable variations. For the lander altitudes at 1 and 3 meters, the bow shock wave is radially upstream, resulting in smoother curves of all variables.

Fig. 11 shows radial profiles of density and velocity magnitude for different lander altitudes and masses. Density has higher values as the lander is closer to the ground at the centerline, inverting positions as the radial distance increases. The plume gas expands more vertically when the lander is closer to the ground, while plume flow expands more radially when it is at higher altitudes. A similar trend occurs for velocity magnitude profiles with some disturbances associated with the shock waves that vary spatial distribution according to the lander altitude.

These variations in velocity and density of the plume emphasize how particle transport strongly depends on local flow conditions. Particles may quickly accelerate due to high local density and velocity flow conditions, maintaining high-speed trajectories due to the quick reduction in the plume density, as shown in the curves in Figs. 10–11.

4.2. Particle motion

Plume ejecta trajectories are highly dependent on the particle size and its initial radial position. Large particles are less likely to be transported by the high-velocity plume flow. Also, particles located further from the centerline experience gas flow with lower density, consequently lower drag force.

Fig. 12 shows the trajectories of the smallest particle size ($D_p = 10^{-6}$ m), initiated at different radial positions, represented by different line colors. Particles are transported by rocket plume flow caused by different lander altitudes and masses. In general, the trajectories for the smallest particle are straight lines within the numerical domain, except for a few cases, where the particles present either one collision with the bottom surface before following a nearly straight line trajectory or remain below the high-velocity region of the rocket plume. However, as the particle size increases, parabolic trajectories occur within the numerical domain due to the prevalence of weight over drag. Fig. 13 summarizes how the particle trajectory is affected by the particle size for a 40-ton lander at 1 m in altitude. Particle size presents similar trends on trajectories for different lander masses and altitudes. As the particle size increases, weight force becomes more prevalent over drag, making particles to impact on the bottom surface and eventually remain in a region of low plume velocity.

On the outlet surfaces of the numerical domain, particles follow a ballistic trajectory, with negligible drag force accelerating them. Due to the negligible aerodynamic forces, particle conditions leaving the numerical domain can be used to estimate particle variables far away from the impingement point, such as particle velocity, kinetic energy, distance traveled. In Figs. 14 and 15, the values of angle, velocity magnitude, kinetic energy, and momentum of the particles leaving the numerical domain are plotted against particle size for a 11-ton lander at the lowest and highest altitude from the bottom surface, respectively. In these figures, different colors and line types represent different radial

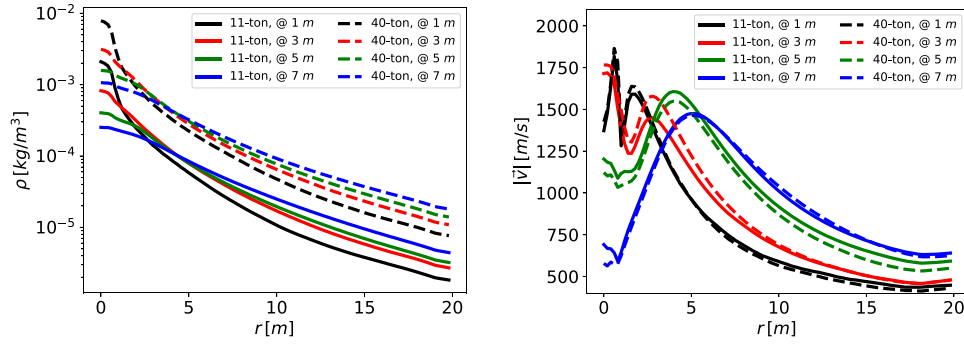


Fig. 11. Radial profiles of density and velocity for different lander masses and altitudes.

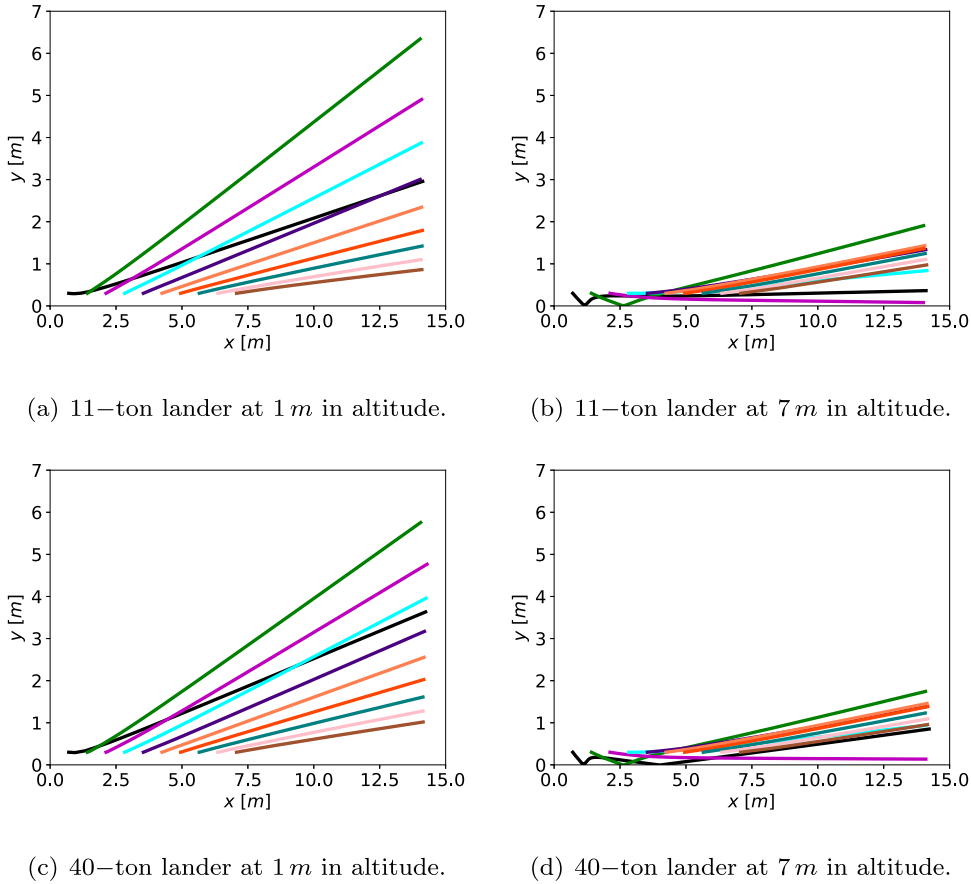


Fig. 12. Particle trajectories for the smallest particle (1 μm) for different lander masses and altitudes. (For interpretation of the references to color in this figure legend, the reader is referred to the web version of this article.)

positions. Particle velocity, momentum, and kinetic energy present linear curves on log-log scales, which is a power-law type relationship between these variables and particle size. Although the particle velocity reduces with particle size, both momentum and kinetic energy increase with particle size due to the dependency of the diameter to the third order. The angle of particles leaving the domain varies with the initial position, remaining constant for a wide range of small particles. The largest particles are more inertial and heavier, making them bounce on the bottom surface. For this reason, these particles present oscillatory ejecta angle, which does not allow functional relation between particle angle and size.

Similar to the plots for the 11-ton lander, Figs. 16 and 17, present the particle angle, velocity magnitude, kinetic energy, and momentum for a 40-ton lander at the lowest and highest altitude from the bottom

surface, respectively. For the 40-ton lander case, particle variables have similar trends to those for the 11-ton lander case. Due to the higher density and velocity of the gas flow, particles accelerated to higher speeds compared to the 11-ton case. Particle angles in the 40-ton case did not vary significantly compared to 11-ton case. In both situations, the initial particle position presented higher influence on particle angle. In general, particle angles are higher as they are close to the shock wave reflection, after the bow shape shock.

Particle velocity achieved a maximum of 755 m/s for the case of a 40-ton lander with the smallest particle size initially placed at one meter from the centerline for the conditions considered in this study. It is important to mention that crater formation, particle lifting mechanisms, and flow instabilities would carry particles to high-speed regions in the flow. Particles at those regions would reach higher speeds

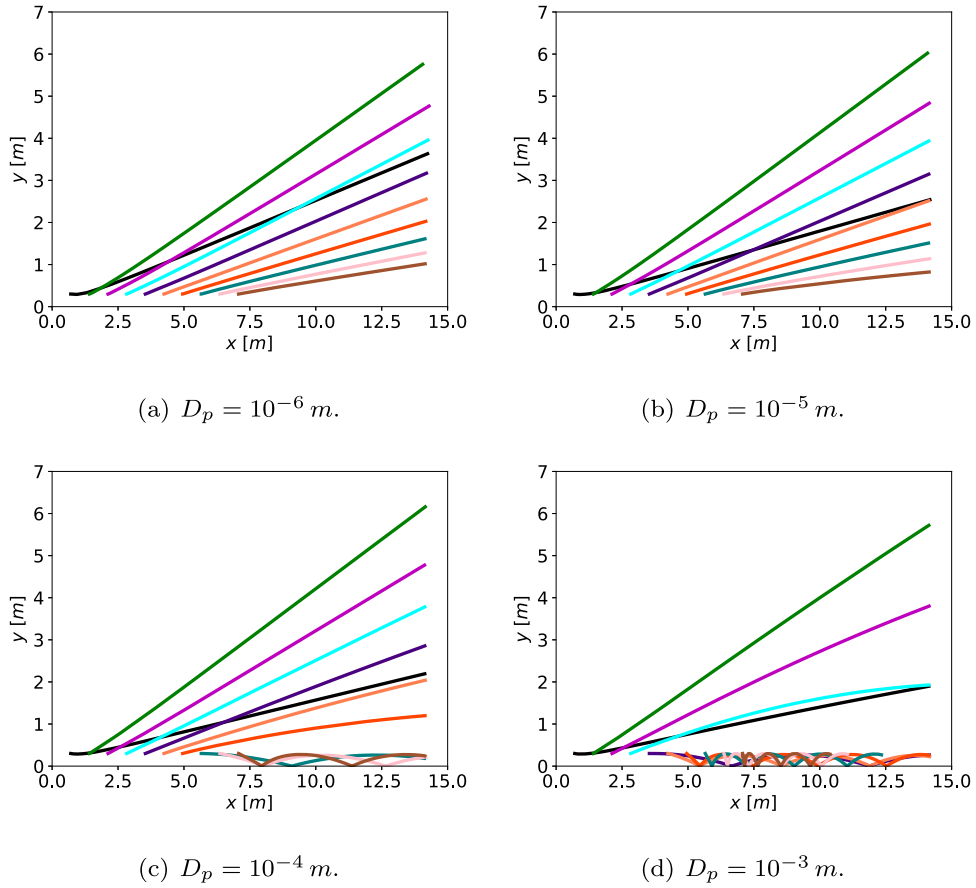


Fig. 13. Particle trajectories of different particle sizes for a 40-ton lander at 1 m in altitude.

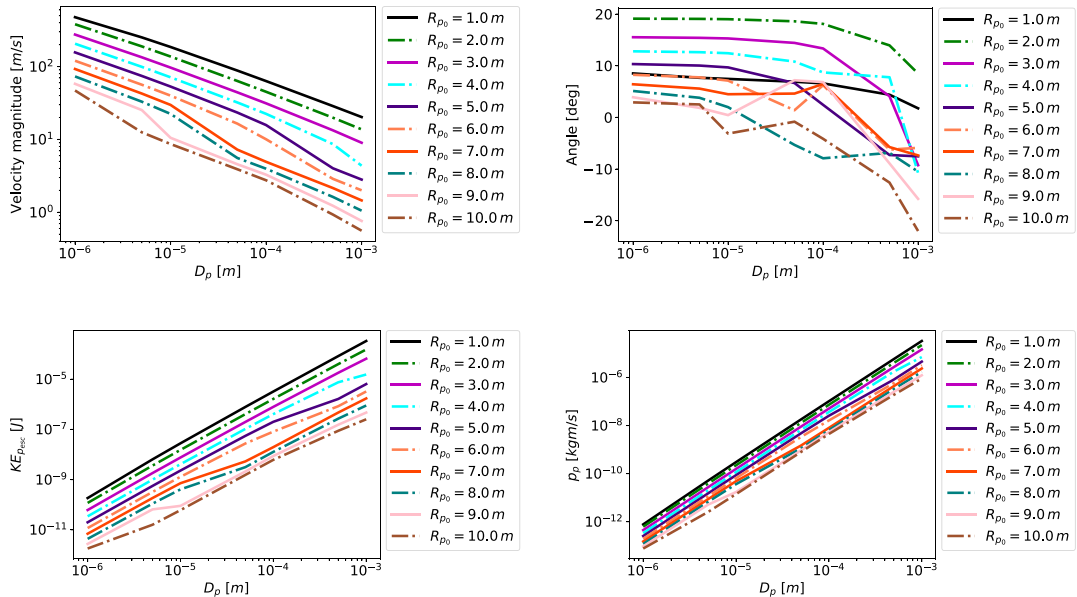


Fig. 14. Dependency of particle variables with particle size and initial radial position for a 11-ton lander at 1 m in altitude. (For interpretation of the references to color in this figure legend, the reader is referred to the web version of this article.)

and angles. Moreover, large particles reaching high dense and speed flow regions would result in a ejecta with high kinetic energy that could damage instruments from nearby and far away structures, given that once accelerated and out of the plume region, these particles would travel with no resistance. Despite the simplifications from the

current model, these predictions provide a first order approximation of particle velocity and trajectory directly related to flat landing surfaces, and minimum estimations of the potential damage caused by particles transported by rocket plumes from such lander sizes.

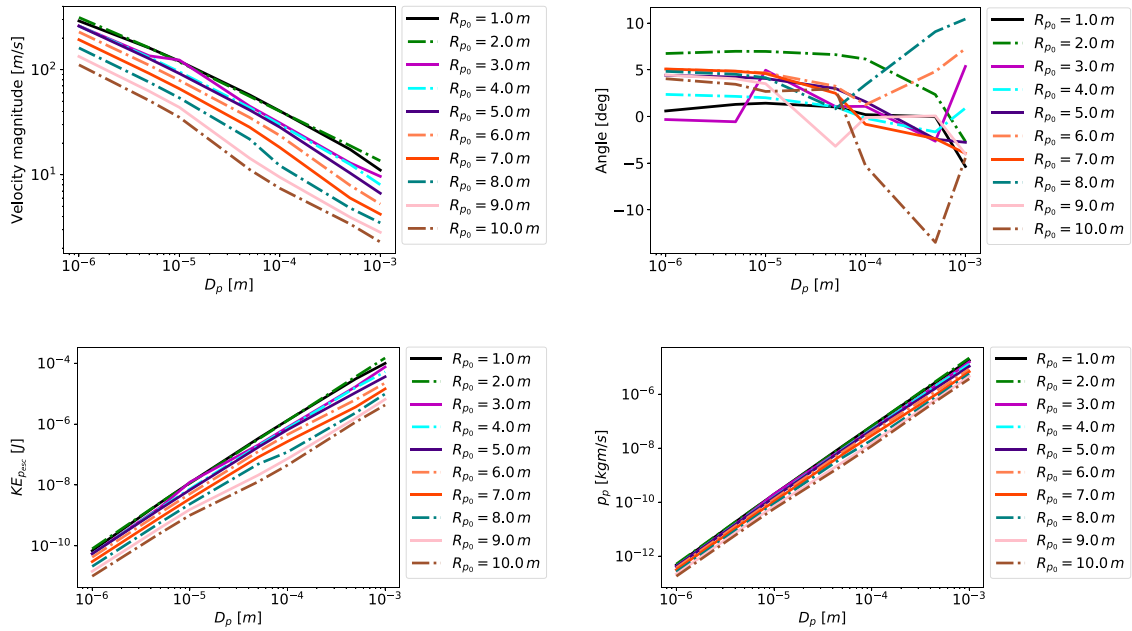


Fig. 15. Dependency of particle variables with particle size and initial radial position for a 11-ton lander at 7 m in altitude. (For interpretation of the references to color in this figure legend, the reader is referred to the web version of this article.)

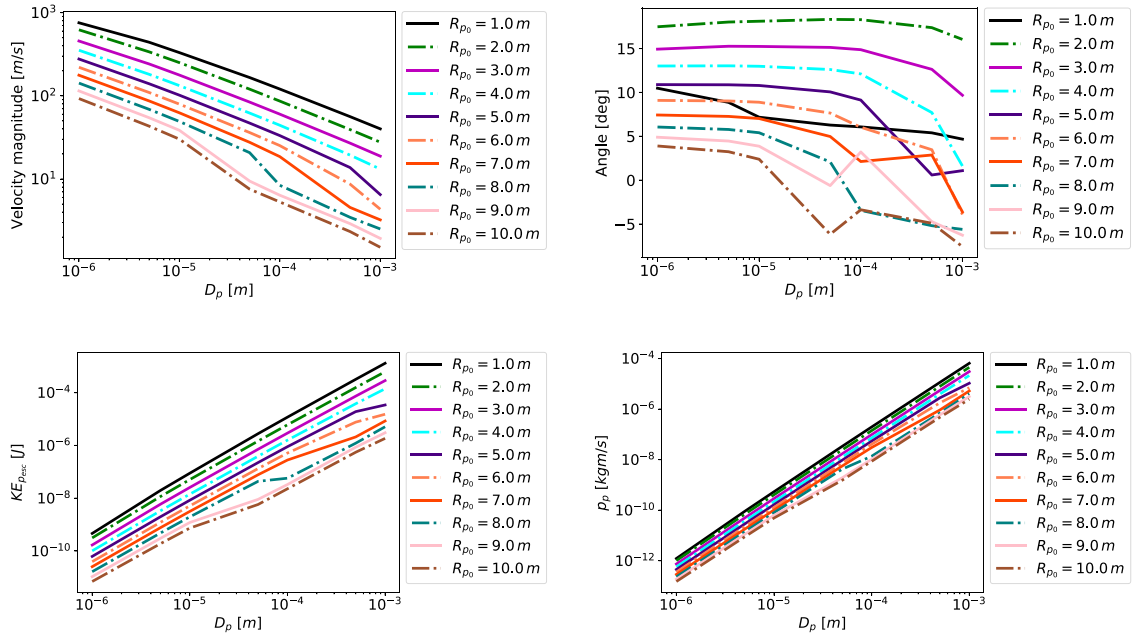


Fig. 16. Dependency of particle variables with particle size and initial radial position for a 40-ton lander at 1 m in altitude.

4.3. Particle velocity correlation

A relational function can estimate particle velocity based on lander and particle characteristics. A mathematical correlation for particle velocity is critical to provide initial estimates and analysis associated with potential damage caused by the regolith ejecta due to a rocket lander descending on the Moon.

By examining the relations between particle velocity magnitude and other variables (particle size and initial position, and lander mass and altitude) associated with the particle–plume flow interactions, we determine a correlation that describes the behavior of particle velocity with those variables.

Considering particle diameter, we used a power-law fitting relation based on the trend of the curves, as depicted in Figs. 14–17.

The particle velocity follows a Gaussian with the particle initial radial position for the smallest particle. A bi-modal Gaussian curve appears for higher lander altitudes. Hence, we considered a direct factor of lander altitude in one Gaussian curve to predict the bi-modal Gaussian curve transition. The lander altitude appears as an indirect factor in the magnitude of the proposed correlation because as the lander approaches the ground surface, the particles assume higher velocities.

In terms of the lander mass, particle velocity was approximated using a power-law relation factoring the correlation. The chosen format of the equation to correlate particle velocity magnitude, $|\vec{v}_p|$ with particle diameter, d_p , particle initial radial position, $r_{p,0}$, lander altitude,

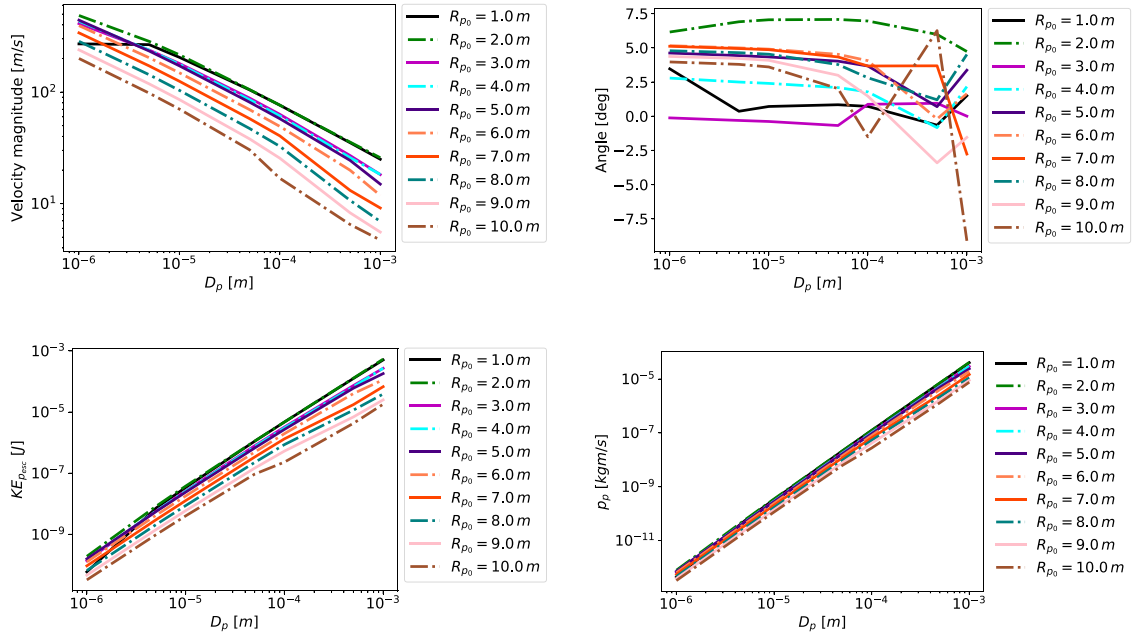


Fig. 17. Dependency of particle variables with particle size and initial radial position for a 40-ton lander at 7 m in altitude.

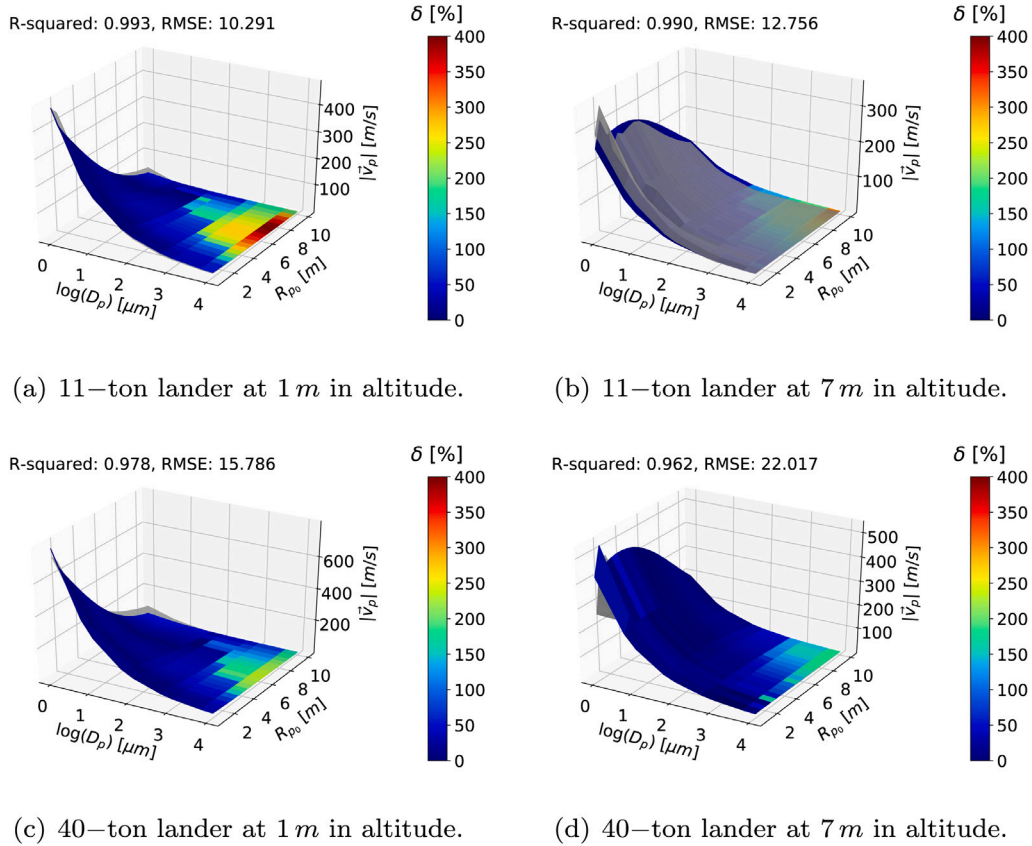


Fig. 18. Comparison of particle velocity magnitude between the simulations and correlation.

l_h , and lander mass, l_m is presented in Eq. (8),

$$|\vec{v}_p|(d_p, r_{p,0}, l_h, l_m) = l_m^{c_1} l_h^{-c_2} d_p^{-c_3} \left\{ c_4 l_h \exp \left[-\frac{(r_{p,0} - (l_h - c_5))^{2.0}}{2.0 c_6^{2.0}} \right] + \exp \left[-\frac{(r_{p,0} - (l_h^{c_7} - c_8))^{2.0}}{2.0 c_9^{2.0}} \right] \right\}. \quad (8)$$

A nonlinear least-squares regression resulted in the coefficient values presented in the Table 2. This table includes the standard deviation, σ , associated with each coefficient obtained through the nonlinear least squares regression. This regression presents overall root mean squared error $RMSE = 18.170$ and coefficient of determination $R^2 = 0.971$.

Table 2

Coefficient values of the particle velocity correlation.

| x | 1 | 2 | 3 | 4 | 5 | 6 | 7 | 8 | 9 |
|------------|-------|-------|-------|-------|-------|-------|-------|-------|-------|
| c_x | 1.362 | 0.415 | 3.718 | 5.084 | 1.846 | 0.770 | 0.62 | 0.400 | 0.695 |
| σ_x | 0.007 | 0.003 | 0.096 | 0.056 | 0.026 | 0.030 | 0.000 | 0.006 | 0.031 |

Fig. 18 depicts the surface curves of particle velocity magnitude from the actual numerical simulations (gray color) and the correlation equation, Eq. (8), with the coefficients presented in Table 2. This figure includes $RMSE$ and R^2 values for each lander mass and altitude pair. The proposed correlation for a 40-ton lander at 2 m in altitude presented the worst agreement with the numerical results, with $RMSE = 29.272$ and $R^2 = 0.925$. The best agreement between the proposed correlation and the numerical data was achieved for an 11-ton lander at 1 m, with $RMSE = 10.291$ and $R^2 = 0.993$.

In general, the fitting curves capture the bi-modal behavior of the particle velocity associated with lander altitude. Moreover, a power-law factor, multiplying the Gaussian curves, accurately describes the relationship between particle velocity and particle size. The difference of particle velocity between the numerical data and curve fitting is relatively low for the majority of particle size and initial position ranges, except for larger particles and fewer points for small particle size and particle positions below $R_{p0} < 3.0$.

We propose this correlation as an input to higher-order modeling to rapidly predict how far the ejecta will go during lunar landings. The estimation of particle's velocity and distance serve as initial parameters to predict how much damage that particles ejected by a lander would cause to surrounding infrastructures.

5. Final remarks

This work presents numerical estimations of the lunar regolith particle motion resulting from plume interaction for different lander masses and altitudes. We used DSMC method to solve the rocket plume flow. The plume flow characteristics agree well with the expected flow results in a vacuum environment, such as the lunar environment. Due to the flow conditions, for 11 and 40 ton landers, a significant part of the numerical domain resulted in local Knudsen numbers beyond the continuum hypothesis validity. These results emphasized the requirement of using a Boltzmann equation method-based approach, such as the DSMC method. Statistical parcels representing the molecules of the combustion products of the propellant N_2O_4 + Aerozine 50 were solved to provide mean flow fields, such as velocity, pressure, temperature, density.

Shear stress on the bottom surface was compared with the Roberts [30] model, presenting similar trends. Compared to the predictions from Roberts [30] and Morris et al. [11], in the present simulations, the shear stress peak was not related to the altitude, which might be associated with the low lander altitudes considered in the present study. For lower altitudes, the jet impinges more perpendicularly to the surface. Thus, variations in the shear stress peak are less dependent on lander altitude.

We solved regolith particle trajectories using a one-way coupled simulation, including weight and drag forces. Particle velocity is directly associated with the quick expansion of the rocket plume flow, particle initialization, and size. Since all particles were inserted into the plume flow at 0.3 m from the bottom surface, they did not reach high-velocity plume regions, higher than 2000 m/s. We consider that particle lifting mechanisms are responsible for transporting particles to high-velocity plume regions. Future research should improve our understanding of the particle lifting mechanisms in the boundary layer and provide solutions to mitigate damage caused by particle blasting.

Using a broad range of particle sizes and positions, different lander altitudes and masses, we derive a convenient correlation for particle velocity based on numerical data fitting. This correlation presents a

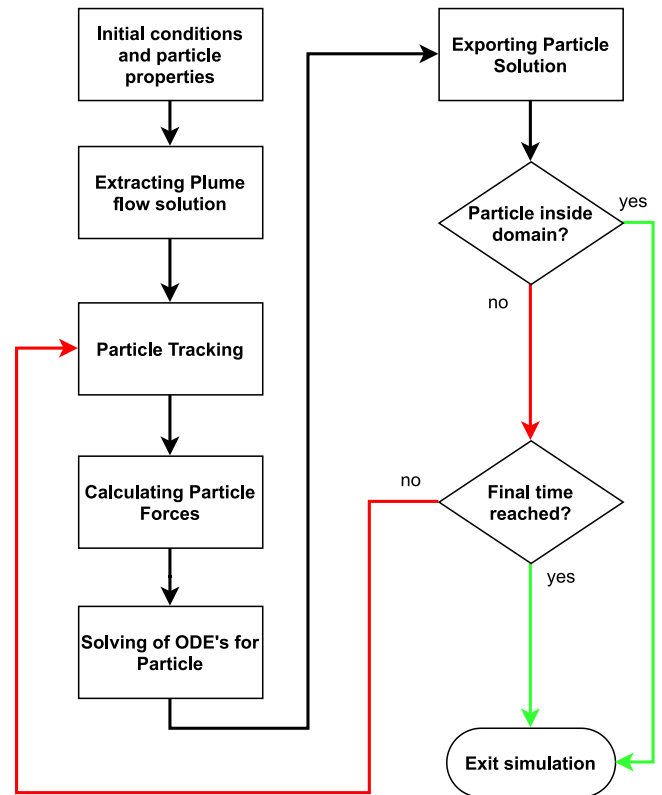


Fig. A.1. Flow chart of the numerical code used to solve the particle transport.

low overall deviation from the numerical simulations, providing a first-order estimation for the ejected particle velocity. Our particle velocity correlation is useful to predict potential damage caused by lunar regolith ejecta in a space vehicle descending to surrounding structures.

Declaration of competing interest

The authors declare that they have no known competing financial interests or personal relationships that could have appeared to influence the work reported in this paper.

Acknowledgments

The authors acknowledge the University of Central Florida Advanced Research Computing Center for providing computational resources and support that have contributed to results reported herein. URL: <https://arcc.ist.ucf.edu>

This research was supported by NASA Grant Number 80NSSC20M0012.

Appendix. Particle transport algorithm

Fig. A.1 shows the flow chart of the particle transport solver implemented in python. After setting the initial conditions and particle properties, the code reads the plume flow solution only once since we considered one-way coupling between gas flow and particulate. Then, the code finds the flow cell that contains the particulate to calculate the particle forces using particle position and plume flow data. In the following, it solves particle velocity and position using Runge-Kutta 4th order. For a pre-selected number of time-steps, we export particle solutions for analysis. The simulation proceeds if the particle is inside the numerical domain; otherwise, it finishes. The simulations loop back to particle tracking until it reaches the final time.

References

- [1] T. Spohn, D. Breuer, T. Johnson, *Encyclopedia of the Solar System*, third ed., Elsevier, 2014, p. 1336.
- [2] S. Li, P.G. Lucey, R.E. Milliken, P.O. Hayne, E. Fisher, J.P. Williams, D.M. Hurley, R.C. Elphic, Direct evidence of surface exposed water ice in the lunar polar regions, *Proc. Natl. Acad. Sci. USA* 115 (36) (2018) 8907–8912, <http://dx.doi.org/10.1073/pnas.1802345115>.
- [3] J.D. Alexander, W.M. Roberts, R.F. Scott, P.R. Coulson, *Soil Erosion by Landing Rockets*, NASA Engineering Report No. 1301 (NAS9-4525), 1966.
- [4] E.M. Christensen, S.A. Batterson, H.E. Benson, R. Choate, R.E. Hutton, L.D. Jaffe, R.H. Jones, H.Y. Ko, F.N. Schmidt, R.F. Scott, R.L. Spencer, G.H. Sutton, Lunar surface mechanical properties, *J. Geophys. Res.* (1896-1977) 73 (22) (1968) 7169–7192, <http://dx.doi.org/10.1029/JB073i022p07169>.
- [5] C. Immer, P. Metzger, P.E. Hintze, A. Nick, R. Horan, Apollo 12 Lunar Module exhaust plume impingement on Lunar Surveyor III, *Icarus* 211 (2) (2011) 1089–1102, <http://dx.doi.org/10.1016/j.icarus.2010.11.013>.
- [6] M. Mehta, A. Sengupta, M. Pokora, L. Hall, N. Renno, Mars landing engine plume impingement ground interaction, in: *Earth and Space 2010: Engineering, Science, Construction, and Operation in Challenging Environments*, 2010, pp. 143–157.
- [7] P.T. Metzger, X. Li, C.D. Immer, J.E. Lane, ISRU implications for lunar and martian plume effects, in: 47th AIAA Aerospace Sciences Meeting including the New Horizons Forum and Aerospace Exposition, 2009, pp. 1–19, <http://dx.doi.org/10.2514/6.2009-1204>.
- [8] R.A. Bagnold, *The Physics of Blown Sand and Desert Dunes*, Dover, 2005, p. 336.
- [9] R.F. Scott, H.Y. Ko, Transient rocket-engine gas flow in soil, *AIAA J.* 6 (2) (1968) 258–264, <http://dx.doi.org/10.2514/3.4487>.
- [10] P.T. Metzger, C.D. Immer, C.M. Donahue, B.T. Vu, R.C. Latta, M. Deyo-Svendsen, Jet-induced cratering of a granular surface with application to lunar spaceports, *J. Aerosp. Eng.* 22 (1) (2009) 24–32, [http://dx.doi.org/10.1061/\(ASCE\)0893-1321\(2009\)22:1\(24\)](http://dx.doi.org/10.1061/(ASCE)0893-1321(2009)22:1(24)).
- [11] A.B. Morris, D.B. Goldstein, P.L. Varghese, L.M. Trafton, Plume impingement on a dusty lunar surface, *AIP Conf. Proc.* 1333 (PART 1) (2011) 1187–1192, <http://dx.doi.org/10.1063/1.3562805>.
- [12] J.E. Lane, P.T. Metzger, Ballistics model for particles on a horizontal plane in a vacuum propelled by a vertically impinging gas jet, *Particul. Sci. Technol.* 30 (2) (2012) 196–208, <http://dx.doi.org/10.1080/02726351.2011.554968>.
- [13] P. Liever, A. Tosh, R. Arslanbekov, S. Habchi, Modeling of rocket plume impingement flow and debris transport in lunar environment, in: 50th AIAA Aerospace Sciences Meeting including the New Horizons Forum and Aerospace Exposition, 2012, p. 22.
- [14] X. He, B. He, G. Cai, Simulation of rocket plume and lunar dust using DSMC method, *Acta Astronaut.* 70 (2012) 100–111, <http://dx.doi.org/10.1016/j.actaastro.2011.07.014>.
- [15] A.B. Morris, D.B. Goldstein, P.L. Varghese, L.M. Trafton, Approach for modeling rocket plume impingement and dust dispersal on the moon, *J. Spacecr. Rockets* 52 (2) (2015) 362–374, <http://dx.doi.org/10.2514/1.A33058>.
- [16] Y. Li, D. Ren, Z. Bo, W. Huang, Q. Ye, Y. Cui, Gas-particle two-way coupled method for simulating the interaction between a rocket plume and lunar dust, *Acta Astronaut.* 157 (December 2018) (2019) 123–133, <http://dx.doi.org/10.1016/j.actaastro.2018.12.024>.
- [17] A. Rahimi, O. Ejtehadi, K.H. Lee, R.S. Myong, Near-field plume-surface interaction and regolith erosion and dispersal during the lunar landing, *Acta Astronaut.* 175 (May) (2020) 308–326, <http://dx.doi.org/10.1016/j.actaastro.2020.05.042>.
- [18] O. Ejtehadi, R.S. Myong, A modal discontinuous Galerkin method for simulating dusty and granular gas flows in thermal non-equilibrium in the Eulerian framework, *J. Comput. Phys.* 411 (2020) 109410, <http://dx.doi.org/10.1016/j.jcp.2020.109410>.
- [19] A.K. Chinnappan, R. Kumar, V.K. Arghode, Modeling of dusty gas flows due to plume impingement on a lunar surface, *Phys. Fluids* 33 (5) (2021) <http://dx.doi.org/10.1063/5.0047925>.
- [20] J.H. Ferziger, M. Peric, R.L. Street, *Computational Methods for Fluid Dynamics*, fourth ed., Springer, 2002, p. 606.
- [21] G.A. Bird, *Molecular Gas Dynamics and the Direct Simulation of Gas Flows*, Oxford Science Publications, 1994, p. 458.
- [22] J.E. Lane, P.T. Metzger, C.D. Immer, X. Li, Lagrangian trajectory modeling of lunar dust particles, in: *Earth and Space Conference 2008: Proceedings of the 11th Aerospace Division International Conference on Engineering, Science, Construction, and Operations in Challenging Environments*, Vol. 323, 2008, pp. 1–9, [http://dx.doi.org/10.1061/40988\(323\)3](http://dx.doi.org/10.1061/40988(323)3).
- [23] C. Immer, J. Lane, P. Metzger, S. Clements, Apollo video photogrammetry estimation of plume impingement effects, in: *Earth & Space 2008*, Vol. 214, American Society of Civil Engineers, Reston, VA, 2008, pp. 1–10, [http://dx.doi.org/10.1061/40988\(323\)1](http://dx.doi.org/10.1061/40988(323)1), URL: <http://ascelibrary.org/doi/10.1061/40988%28323%291>.
- [24] R.A. Braeunig, Rocket propellants, in: *Basics of Space Flight: Rocket Propellants*, 2008, URL: <http://www.braeunig.us/space/propel.htm>.
- [25] C. White, M.K. Borg, T.J. Scanlon, S.M. Longshaw, B. John, D.R. Emerson, J.M. Reese, Dsmcfoam+: An OpenFOAM based direct simulation Monte Carlo solver, *Comput. Phys. Comm.* 224 (2018) 22–43, <http://dx.doi.org/10.1016/j.cpc.2017.09.030>.
- [26] C. Borgnakke, P.S. Larsen, Statistical collision model for Monte Carlo simulation of polyatomic gas mixture, *J. Comput. Phys.* 18 (1975) 405–420.
- [27] H. Jasak, A. Jemcov, Ž. Tuković, OpenFOAM: A C++ library for complex physics simulations, in: *International Workshop on Coupled Methods in Numerical Dynamics*, Vol. m, 2007, pp. 1–20.
- [28] S.I. Popel, L.M. Zelenyi, A.P. Golub', A.Y. Dubinskii, Lunar dust and dusty plasmas: Recent developments, advances, and unsolved problems, *Planet. Space Sci.* 156 (February) (2018) 71–84, <http://dx.doi.org/10.1016/j.pss.2018.02.010>.
- [29] F.E. Lumpkin III, J. Marichalar, A. Piplica, Plume impingement to the lunar surface: A challenging problem for DSMC, *Chem. Phys. Lett.* 289 (1–2) (2007) [http://dx.doi.org/10.1016/S0009-2614\(98\)00399-6](http://dx.doi.org/10.1016/S0009-2614(98)00399-6).
- [30] L. Roberts, The interaction of a rocket exhaust with the lunar surface, in: *The Fluid Dynamics Aspects of Space Flight; Proceedings*, Vol. 2, 1966, p. 1.